A&A 427, 1055–1064 (2004)
DOI: 10.1051/0004-6361:20040345

Astronomy & Astrophysics

Can ion-neutral damping help to form spicules?

II. Random driver

R. Erdélyi and S. P. James

Space and Atmosphere Research Center, Department of Applied Mathematics, University of Sheffield, The Hicks Building, Hounsfield Road, Sheffield S3 7RH, UK
e-mail: robertus@shef.ac.uk; s.p.james@shef.ac.uk

Received 26 February 2004 / Accepted 10 August 2004

Abstract. The possible mechanism of generation of spicules by Alfvénic disturbances is studied in dissipative MHD where dissipation is mainly caused by ion-neutral collision damping, as suggested by Haerendel (1992).
Ion-neutral damping becomes non-negligible in the upper chromosphere at high cyclic frequencies of typically greater than 0.1 Hz, and the potential role played by this effect in both forming and supporting solar spicules is investigated.
The propagation of *randomly* generated Alfvénic disturbances on vertically open solar magnetic flux tubes is considered. The flux tubes are taken to be axisymmetric and initially untwisted with the field strength declining from 1600 G in the photosphere to 20 G in the corona. Their propagation is investigated by numerically solving a set of fully nonlinear, dissipative 1.5D MHD equations with waves being generated by a continuous random driver introduced into the equation of angular momentum in the low atmosphere of the Sun.
This work is a continuation of James et al. (2003) which studied the results for a continuous, monochromatic sinusoidal driver. As with the previous study, spicule-like structures were formed. The formation was again found to be primarily caused by the impact of a series of slow shocks generated by the continuous interaction between the upward propagating driven disturbance and the downward propagating disturbances reflected by the transition region. The formation was aided by the increased thermal pressure gradient caused by Joule heating due to ion-neutral collisions. There is some indication that an analogue of the momentum transfer effect suggested by Haerendel (1992) for simple sinusoidal waves is at work, but this effect on it's own is at best only of a similar order as the reduction in height caused by including damping in the first place. However, the effect is highly sensitive to the level of ionisation and therefore to the energy balance. Including the effects of thermal conduction and radiation may well lead to different results and thus it would be premature to dismiss the mechanism completely at this point. Significant damping and heating was again observed, strengthening the previously made suggestions that ion-neutral damping may play a more important role in the dynamics of the upper chromosphere than normally assumed in numerical simulations (where it is often neglected completely), although a treatment of radiative losses must be included before this can be confirmed. The heating provided by ion-neutral damping may be an appropriate counter to the low temperatures suffered by other mechanisms better able to reproduce spicule dynamics.

Key words. magnetohydrodynamics (MHD) – waves – Sun: transition region – Sun: faculae, plages – Sun: atmosphere – Sun: chromosphere

1. Introduction

Solar spicules are long, thin cylindrical jet-like structures seen above the solar limb and best observed in strong chromospheric emission lines. The majority of observations have been obtained in Hα and it is these spicules that the following refers to, unless otherwise specified. They appear to be guided along the intense magnetic flux tubes at supergranule boundaries. As the spatial resolution of observing instruments has improved, estimates of their width have reduced. Lynch et al. (1973) obtained a mean width of 950 km with over 80% having widths in the range 500–1250 km. Later, Nishikawa (1988) found an average of 615 km with the majority below 900 km. It seems likely that a sizable number of "wide" spicules are actually unresolved bundles of thinner spicules. Whatever their true dimensions, it is certainly true to say that spicule widths are of a similar order to the spatial resolution of observational instruments and this is probably a major factor in the disagreement in observed spicule properties. Lynch et al. (1973) reports a decrease in spicule width with height which is also reported by Nishikawa (1988) but in both cases the decrease is so slight that the spicule is to all intents and purposes constant in diameter. Whilst magnetic flux tubes must widen considerably in going from photospheric field strengths in excess of 1000 G to coronal values of a few tens of Gauss, most of this widening has already occurred by the transition region heights at which

spicules can first be separated from the surrounding continuum. Therefore a constant diameter spicule is not in contradiction with the assumption that spicules are guided along magnetic flux tubes.

Dynamically, spicules are short-lived events comprising an apparent upward motion of chromospheric material at speeds of around 25 km s^{-1} to heights of 6500–9500 km after which most are seen to descend with similar velocities but some fade from view. The lower end of this height range represents heights above the limb at which individual spicules typically become clearly distinguishable from the surrounding continuum. It is likely that smaller spicules exist, but in such large numbers they cannot be individually distinguished. Typical lifetimes (for which the spicule is observable above the continuum) are around 10 min. That some spicules fade from view rather than descend is noteworthy. One possible explanation is that the plasma is heated and "evaporated" into the transition region and corona, thus vanishing from Hα lines. Since the globally averaged upward mass flux of spicules is some 100 times the coronal mass-loss rate (Beckers 1972), it is likely spicules play an important role in the solar atmospheric mass-balance. The possibility of spicular evaporation has been investigated by Budnik et al. (1998) who conclude that at least some spicular material is heated to transition region temperatures and evaporates into the corona.

The time evolution of the spicule velocity is unclear. The tendency in the literature is to assume the rise is non-ballistic in nature. Nishikawa (1988) shows that observational evidence is actually inconclusive on this point because the regions of high velocity lie below the observable level at the solar limb. However, one strong argument against a ballistic model is that the required initial velocities of 80 km s^{-1} have not been observed on the disk. Both Hasan & Keil (1984) and Pasachoff et al. (1968) report seeing variations in the velocity profiles propagating at greater than 300 km s^{-1} between about 2000 km and 4000 km in height. This is much greater than the chromospheric sound speed but similar to the Alfvén speed, suggesting acceleration of spicular material is driven by a magnetic mechanism.

Many spicule emission spectra are inclined to the spectrograph dispersion (Beckers 1972) which can be attributed to rotation of the spicule. Pishkalo (1994) found that about half of all spicules showed spectral tilts at some point in their lifetimes and that rotation must be in the range of 20–35 km s^{-1} to fit the observed spectral profiles.

Under spicular conditions, deviations from LTE are significant. This is another source of disagreement between observers as involved non-LTE calculations are required to interpret spicule line information. Beckers (1972) found temperatures steadily increased from 9000 K at 2000 km to 16 500 K at the top of the spicule. Matsuno & Hirayama (1988) find much lower temperatures of 5000–8000 K and also find a decrease in temperature from 2200–3000 km in height before the temperature starts to increase. It is probably reasonable to say that spicule temperatures are of typical chromospheric values and that the temperature rises along most of the spicule length. There is less disagreement about spicule densities. Beckers (1972) finds electron densities of $3–15 \times 10^{16}$ m^{-3} with the value decreasing over the whole spicule length. Mass densities are about 3×10^{-10} kg m^{-3}, which is typical of upper chromospheric densities. Both the temperature and the density profiles are very flat; the density scale height is several thousand kilometres compared with a few hundred for the upper chromosphere when in hydrostatic equilibrium.

Spicule velocities are comparable with the local sound speed so that any model must necessarily take account of non-linear effects. As a consequence, the focus has shifted toward numerical modeling as computers have become sufficiently advanced to handle the non-linear MHD equations. Sterling (2000) gives an excellent review of the current state of progress of numerical models. Almost exclusively, these models involve a deposition of energy and/or some artificial driving force in the lower atmosphere of a rigid flux tube. Suematsu et al. (1982) investigated the effect of a sudden pressure enhancement in the low chromosphere in a flux tube of constant cross-section. The initial pressure pulse nonlinearly steepens into a gasdynamic shock which impacts on the transition region, pushing it upward. This model is ballistic in nature and predicts initial velocities of around 60 km s^{-1}. As mentioned above, such large velocities have not been observed on the disk. The model recreates other spicule properties reasonably well although the temperatures are very much at the lower end of observations. The model is adiabatic and it seems likely that inclusion of radiation losses would reduce temperatures below observational constraints.

Hollweg (1982) investigated a weak velocity pulse in a flux tube with expanding cross section. The velocity perturbation results in an acoustic gravity wave train consisting of a wave front followed by an oscillating wake as described in the linear regime. Both the initial wave front and the oscillating wake steepen into a series of slow shocks, referred to as *rebound shocks* since they form when falling plasma uplifted by previous shocks rebounds back upward. The initial and rebound shocks continually impact the transition region resulting in intermittent rises. Since the shocks are weaker than in the pressure pulse model of Suematsu et al. (1982), the high velocities are not seen. It is argued that the intermittent velocity would fit the non-ballistic approximately constant velocity profile observed under low temporal resolution. A number of follow up investigations of this rebound shock model have been conducted by various authors; Sterling & Hollweg (1988) extended the original calculations in time and parameter space, Sterling & Mariska (1990) added radiation and heat conduction and Cheng added the effects of ionisation and variable molecular weight in a series of papers (Cheng 1992a–c). Incorporation of radiative losses tends to reduce the height of the structures formed. As yet, observations are unable to either confirm or refute the testable prediction of these models, namely the intermittent velocities of the spicule tops. Future higher spatial and temporal resolution observations will hopefully clarify this issue.

De Pontieu et al. (2003) observed oscillations of the upper transition region in active region plage which showed a correlation with p-mode oscillations in the photosphere. Numerical simulations related to these observations have been carried out by De Pontieu et al. (2004) and seem to successfully recreate

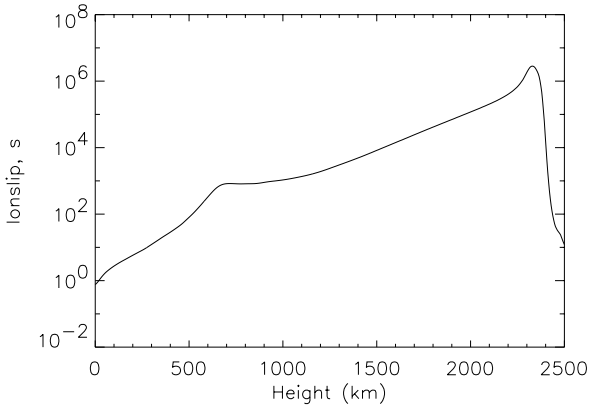

Fig. 1. Ion slip profile for the case of 20 G coronal field.

the low-lying spicules observed on the disk in active region plage.

The first MHD spicule simulations were carried out by Hollweg et al. (1982) who studied the evolution of a low-frequency Alfvénic pulse launched from the photosphere. This pulse evolved into an MHD fast-mode shock which moved the transition region upward. The structure formed was too short and cool to be identified with a spicule before the inclusion of radiative losses (which have been shown for other formation mechanisms to impede spicule formation). Kudoh & Shibata (1999) studied the effect of a series of randomly generated Alfvénic pulses. They found that spicular structures with heights of 5000 km could be generated but again their model did not incorporate radiation losses which can be expected to reduce heights.

2. The possible role of ion-neutral damping in spicule formation

The presence of a magnetic field forces electrons and ions to gyrate about that field. As a result of this reduction in mobility, the conductivity perpendicular to the magnetic field is reduced. Following Cowling (1976), a more generalised form of Ohm's law can be derived:

$$\boldsymbol{E} = -\boldsymbol{v} \times \boldsymbol{B} + \frac{1}{\sigma_0} \left(\boldsymbol{J} + \beta_\mathrm{e} \boldsymbol{J} \times e_B + s\, \boldsymbol{e_B} \times (\boldsymbol{J} \times \boldsymbol{e_B}) \right), \qquad (1)$$

where σ_0 is the electrical conductivity. $\beta_\mathrm{e} = \omega_\mathrm{e}/\nu_\mathrm{eH}$ being the electron gyrofrequency divided by the collision frequency between electrons and heavy particles, is a measure of the typical number of times an electron can gyrate around the magnetic field between collisions. $s = (\rho/\rho_n)^2 \beta_\mathrm{e}\beta_\mathrm{i}$ is the ion slip and is purely due to the interaction between the ion and neutral fluids. Changes in the magnetic and electric fields impact on the ions directly but are only felt by the neutral fluid due to collisional coupling. The neutral and ion fluids thus "slip" over each other, potentially causing dissipation and heating. This mechanism becomes important if the time scale for changes in the electric and magnetic fields is comparable with the ion-neutral collision time, τ_in.

Figure 1 shows a typical ion slip profile as calculated by our code (details below). Just below the transition region, ion-neutral damping results in a resistivity enhancement of more than 1 million times. It is in the upper chromosphere that the effect first becomes important. One interesting feature is the small region of enhanced ion slip just below the transition region. At this point, the temperature is high enough for the hydrogen to be mostly, but not completely, ionised whilst the helium is predominantly neutral, the most efficient conditions in the solar atmosphere for the mechanism. The ion slip drops off rapidly once the temperature becomes high enough to completely ionise hydrogen in the transition region.

For an undamped wave, the Lorentz force at any given position oscillates symmetrically about zero and the average force over one wave-period is precisely zero. When the wave is damped, the Lorentz force becomes progressively weaker – it still oscillates about zero but with decreasing amplitude. As a result, the net force over one waveperiod is no longer zero and can drive longitudinal motions.

Work by Haerendel (1992) and later by De Pontieu & Haerendel (1998) showed, using the WKB approximation applied to plane parallel linear Alfvén waves, that ion-neutral damping results in a wave period averaged force in the direction of propagation of

$$\overline{F_z} = \rho_\mathrm{n} \overline{v_{1y}^2} \frac{\omega^2}{2\nu_\mathrm{ni} v_\mathrm{A}}, \qquad (2)$$

with an associated wave period averaged energy dissipation of

$$\overline{\dot{\epsilon}} = \rho_\mathrm{n} \overline{v_{1y}^2} \frac{\omega^2}{\nu_\mathrm{ni}} = 2 v_\mathrm{A} \overline{F_z}, \qquad (3)$$

where ω is the angular wave frequency, ν_ni the neutral-ion collision frequency, v_{1y} is the transverse wave velocity, v_A is the Alfvén speed and ρ_n is the neutral density. They speculated that Alfvén waves with frequencies around 0.5 Hz could provide enough upward momentum by this mechanism to support structures with typical spicular parameters against gravity.

De Pontieu (1999) carried out numerical simulations to test this hypothesis. He used a set of essentially 1D *hydrodynamic* wave-period averaged equations which incorporated the vertical magnetic field implicitly by following the evolution along a flux tube of height-dependent cross-section. Transport and damping of Alfvén waves was included without having to resort to 1.5D MHD equations by the addition of an equation of wave action density. The resulting structure and its dynamics showed good agreement with observations. However, in the transition region the density drops and the temperature increases by roughly two orders of magnitude in just 2–300 km whilst the Alfvén speed is around 100 km s^{-1}. The WKB approximation is clearly violated, even at the high frequencies involved. In particular, the steep temperature and density gradients will lead to strong reflection of the Alfvén waves at the transition region and these reflected waves will interact with the upcoming wave train. No account of these reflections was taken by De Pontieu's model. James et al. (2003), hereafter Paper I, extended this work to 1.5D MHD simulations with a simple sinusoidal driver. This work was itself a continuation of preliminary results from James & Erdélyi (2002). Whilst spicule-like structures were formed, it was found that the damping force mechanism, if it was present at all was not a significant contributor. More than half the incident driven wave energy was

reflected by the transition region. The driven upward propagating and reflected wave trains interfered with each other deforming the chromosphere periodically into regions of locally high and low density with a spatial periodicity of half the local Alfvén wavelength at the frequency of the driver. Perturbations in the vertical velocity steepened into slow shocks about these points and the passage of these shocks caused roughly periodic increases in transition region height. Dynamics were largely governed by the strength of these slow shocks which in turn was primarily dependent on the amplitudes of the driven and reflected waves. It was postulated that this effect was a result of the driver and that a random source of Alfvénic disturbances would remove the generation of these slow shocks. This paper presents the results of simulations with such a driver.

3. Governing equations

Following Hollweg (1982), we consider a rigid, vertical, axisymmetric and initially untwisted flux tube. We define a local orthogonal curvilinear coordinate system by z, the distance along a field line, θ, the azimuthal angle about the axis of symmetry and ξ, a coordinate measured in the $\hat{\boldsymbol{z}} \times \hat{\boldsymbol{\theta}}$ direction. We assume axial symmetry,

$$\frac{\partial}{\partial \theta} \equiv 0. \tag{4}$$

Additionally, all motions and gradients perpendicular to the flux tube are suppressed;

$$\frac{\partial}{\partial \xi} \equiv 0,\ v_\xi = B_\xi = 0. \tag{5}$$

This latter assumption, equivalent to assuming horizontal homogeneity since the flux tube we consider is approximately vertical, requires that we study the evolution along field lines close to the tube axis. We consider the system to be adiabatic with the exception of a heating term resulting from ion-neutral damping. The basic MHD equations reduce to the following system:

$$\frac{\partial}{\partial t}\left(\frac{\rho}{B_z}\right) + \frac{\partial}{\partial z}\left(\frac{\rho v_z}{B_z}\right) = 0, \tag{6}$$

$$\frac{\partial}{\partial t}\left(\frac{\rho r v_\theta}{B_z}\right) + \frac{\partial}{\partial z}\left(\frac{\rho r v_\theta v_z}{B_z}\right) = \frac{1}{\mu_0}\frac{\partial}{\partial z}(rB_\theta), \tag{7}$$

$$\frac{\partial}{\partial t}\left(\frac{\rho v_z}{B_z}\right) + \frac{\partial}{\partial z}\left(\frac{\rho v_z^2}{B_z}\right) =$$

$$-\frac{1}{B_z}\left[\frac{\partial p}{\partial z} + \rho g - \frac{v_\theta^2}{r}\frac{\partial r}{\partial z} + \frac{B_\theta}{\mu_0 r}\frac{\partial}{\partial z}(rB_\theta)\right], \tag{8}$$

$$\frac{\partial}{\partial t}\left(\frac{B_\theta}{rB_z}\right) + \frac{\partial}{\partial z}\left(\frac{B_\theta v_z}{rB_z}\right) = \frac{\partial}{\partial z}\left(\frac{v_\theta}{r}\right) + \frac{1}{\mu_0}\frac{\partial}{\partial z}\left(\frac{s}{B_z r^2 \sigma_0}\frac{\partial}{\partial z}(rB_\theta)\right), \tag{9}$$

$$\frac{\partial}{\partial t}\left(\frac{e}{B_z}\right) + \frac{\partial}{\partial z}\left(\frac{e v_z}{B_z}\right) = -p\frac{\partial}{\partial z}\left(\frac{v_z}{B_z}\right) + \frac{s}{B_z \mu_0^2 \sigma_0 r^2}\left[\frac{\partial}{\partial z}(rB_\theta)\right]^2, \tag{10}$$

$$e = \frac{p}{\gamma - 1} + n_{\rm e}\chi_{\rm H}, \tag{11}$$

where e is the internal energy, the sum of the thermal and ionisation energies. The ionisation energy is only an approximation as it assumes that all electrons result from ionised hydrogen. However, this is a very good approximation as hydrogen is by far the most abundant element in the solar atmosphere and the ionisation energies of the other elements are of the same order as that of hydrogen. It is important to include the ionisation energy as it dominates the thermal energy in the upper chromosphere and in conditions typical of spicules.

4. Details of the numerical simulation

4.1. Ionslip and the ionisation state

The ionslip term is given fully (e.g., Mitchner 1973) by:

$$\nu_{\rm in} = \sum_{\text{ions},\,j}\ \sum_{\text{neutrals},\,k} \frac{\rho_{{\rm i}_j}}{\rho_{\rm i}}\frac{\rho_{{\rm n}_k}}{\rho_{\rm n}}\nu_{{\rm i}_j{\rm n}_k}, \tag{12}$$

where $\rho_{{\rm i}_j}$ is the density of ions of species j, $\rho_{{\rm n}_k}$ is the density of neutrals of species k, $\rho_{\rm i}$ is the total ion density, $\rho_{\rm n}$ is the total neutral density and $\nu_{{\rm i}_j{\rm n}_k}$ is the momentum transfer collision frequency between ions of species j and neutrals of species k. This latter is defined, assuming the species have equal temperature, by:

$$\nu_{12} = n_2\left(\frac{8kTm_2}{\pi m_1\,(m_1 + m_2)}\right)^{1/2}\sigma_{12}, \tag{13}$$

where σ_{12} is the collisional cross-section for collisions between the two species.

At most temperatures, hydrogen is by far the most abundant ion and also the most abundant neutral. Since hydrogen ionises at lower temperatures than helium, at sufficiently high temperatures helium becomes important in the balance of neutrals. Only the hydrogen and helium neutrals need be considered in calculating the ion slip. Since metals in the Sun ionise at lower temperatures than hydrogen, at sufficiently low temperatures hydrogen is no longer the dominant ion. However, at these low temperatures the ion slip is negligible so only hydrogen ions are included in calculating the ion slip. Equation (12) reduces to:

$$\nu_{\rm in} = \left[\frac{1}{\sqrt{2}}n_{\rm HI}\sigma_{\rm HII\,HI} + \sqrt{\frac{4}{5}}n_{\rm HeI}\sigma_{\rm HII\,HeI}\right]\left(\frac{8kT}{\pi m_{\rm H}}\right)^{1/2}. \tag{14}$$

We have taken the values of $\sigma_{\rm HII\,HI} = 5 \times 10^{-19}\,{\rm m}^2$ and $\sigma_{\rm HII\,HeI} = 8 \times 10^{-20}\,{\rm m}^2$ from Osterbrock (1961).

In calculating the ionisation state we closely follow the technique described by De Pontieu (1999). Since $s/\sigma_0 \propto 1/n_{\rm e}$, we include some of the heavy elements in order to provide electrons and prevent the damping and heating becoming unrealistically large at low temperatures. Our model atmosphere consists of hydrogen, helium, magnesium, silicon and iron. With the exception of hydrogen, we assume LTE and use the Saha equation;

$$\frac{n_{j+1}}{n_j}n_{\rm e} = \frac{u_{j+1}}{u_j}2\frac{(2\pi m_{\rm e}k_B T)^{3/2}}{h_3}{\rm e}^{-\chi_j/k_{\rm B}T}, \tag{15}$$

where n_j is the number density of ions in the jth ionisation state, m_e is the electron mass and χ_j is the ionisation energy needed to ionise the jth state. The partition functions are equated with the lowest ground term,

$$u_j = g_{j,0}. \tag{16}$$

For singly ionised elements, Eq. (15) yields for each element, k:

$$n_{i_k} = \frac{n_k}{1 + (n_e/a_k)}, \tag{17}$$

where n_k is the total number density of element k, n_{i_k} is the number density of singly ionised element k, n_e is the total electron density and a_k is the right hand side of Eq. (15).

Both singly and doubly ionised helium are included and some simple algebra yields:

$$n_{\mathrm{HeII}} = \frac{n_{\mathrm{He}}}{(n_e/a_{\mathrm{HeII}}) + 1 + (a_{\mathrm{HeIII}}/n_e)} \tag{18}$$

and

$$n_{\mathrm{HeIII}} = \frac{a_{\mathrm{HeIII}}}{n_e} n_{\mathrm{HeII}}. \tag{19}$$

A non-LTE modification is applied for hydrogen following Brown (1973):

$$\frac{n_{j+1}}{n_j} n_e = \frac{a}{b_1}, \tag{20}$$

where

$$b_1 = \frac{T}{WT_R} \mathrm{e}^{\left[\frac{\chi_H}{4kT}(T/T_R - 1)\right]}. \tag{21}$$

Here $T_R = 5700$ K is the temperature of the photospheric radiation field and $W = 0.5$ is the dilution factor.

Since the plasma is electrically neutral, we obtain an implicit equation for the total electron density which is a function of temperature and density (equivalently total hydrogen number density since we assume no variation with height of relative elemental abundances):

$$n_e = \sum_k n_{i_k} q_{i_k}, \tag{22}$$

where $q_{i_k} = 2$ for doubly ionised helium and 1 for all other species. Equations (11), (22) and the perfect gas law form a closed system of equations in the unknowns p, n_e and T given the known quantities e and n_H. This system is solved iteratively at the beginning of each time step using the quantities in Table 1 for the various atomic parameters.

4.2. Equilibrium conditions

The atmosphere is assumed to be initially in hydrostatic equilibrium:

$$\frac{\partial p}{\partial z} = -\rho g. \tag{23}$$

The perfect gas law:

$$p = (\alpha_1 n_H + n_e)\, kT, \tag{24}$$

Table 1. Atomic parameters of elements in our model from Allen (1963).

Element name	Atomic weight (m_H)	$\log_{10}$ (abund)	χ (eV)	g_0	g_{i0}
H	1	12	13.598	2	1
He	3.97	10.93	24.587	1	2
He^+	3.97		54.416	2	1
Mg	24.11	7.6	7.646	1	2
Si	27.86	7.6	8.151	9	6
Fe	55.41	7.6	7.87	25	30

where n_H is the total hydrogen number density, both ions and neutrals, and $\alpha_1 n_H$ is the number density of all heavy particles. For the solar atmosphere, $\alpha_1 = 1.0852$. The density can then be expressed by

$$\rho = \left(\frac{p}{kT} - n_e\right) \mu m_p, \tag{25}$$

where $\mu = 1.34$ is the mean molecular mass for the solar atmosphere and $m_p = 1.673 \times 10^{-27}$ kg is the mass of a proton. Equations (24) and (25) are then combined to give

$$\frac{\partial p}{\partial z} = -\left(\frac{p}{kT} - n_e\right) \mu m_p g. \tag{26}$$

We introduce regions of suppressed gravity in both the upper and lower regions of the computational domain in order to make Eq. (23) compatible with the flow-through boundary condition, $\frac{\partial}{\partial z} \equiv 0$. This is achieved by fitting the gravitational acceleration profile using cubic functions to ensure continuity up to and including the second order differential. Both of these regions are placed well outside the domain of interest. To obtain the initial atmosphere, Eq. (26) is integrated by the Euler method on a very high resolution grid (a low order scheme is chosen for ease of coding since efficiency is unimportant for this stage),

$$p_{i+1} = p_i + (x_{i+1} - x_i) \times f_i, \tag{27}$$

where p_i is the pressure at the ith gridpoint, x_i is the height of the ith gridpoint and f_i is the right hand side of Eq. (23) evaluated at the ith gridpoint. In order to calculate f_i, we solve the implicit equation for the electron number density, Eq. (22), combined with the perfect gas law using the known values of p (the value of which has to be prescribed at one gridpoint for the method to proceed) and the temperature profile, T, from the VAL IIIc quiet Sun reference atmosphere of Vernazza et al. (1981). For numerical reasons, we integrate from the top of the atmosphere downward. The pressure at the first gridpoint is arbitrary and is chosen in such a way as to give good agreement in the generated pressure and density profiles with the corresponding VAL IIIc profiles in the chromosphere.

For the vertical magnetic field, we take the potential field model for a flux tube at the edge of several supergranular cells from De Pontieu (1996):

$$B = B_{\mathrm{corona}} + \frac{B_{\mathrm{photosphere}}}{\left(1 + (z/R_s)^2\right)^{3/2}}, \tag{28}$$

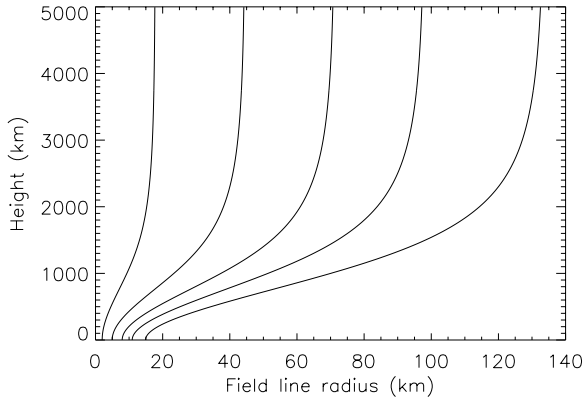

Fig. 2. Field lines of various initial radius for a model magnetic field of 20 G coronal field strength.

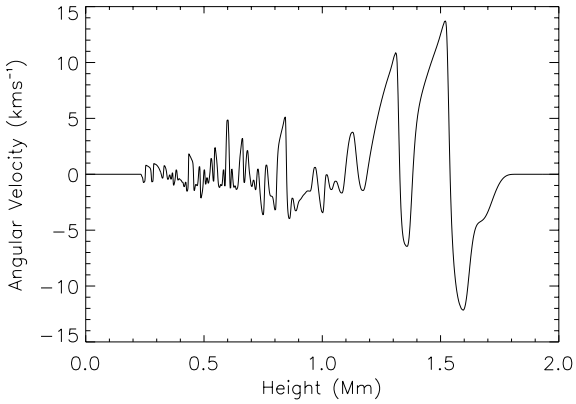

Fig. 3. A snapshot of the angular velocity profile just before the driven Alfvénic disturbances reach the transition region.

where $B_{\rm corona}$ and $B_{\rm photosphere}$ are the coronal and photospheric magnetic fields respectively. $R_{\rm s}$ is a parameter depending on the area of the hexagonal supergranular cells. Figure 2 shows the profile of a number of field lines with $B_{\rm photosphere} = 1600\,{\rm G}$ and $B_{\rm corona}$ with initial radius (radius at $z = 0$) varying from 2−15 km.

The grid spacing is determined in such a way that there are initially at least 50 gridpoints per Alfvén wavelength for 3 s wave period. This means that disturbances with shorter characteristic wave periods are likely to be numerically damped. Because we expect chromospheric material to be ejected upwards, we over-resolve above the transition region to ensure sufficient resolution at all subsequent times in the simulation. We also under-resolve in the low photosphere since we are unconcerned with wave evolution in this region. As well as significantly decreasing the number of gridpoints required and thus the computational time, the resultant numerical damping helps to reinforce the flow-through boundary condition and ensures negligible reflection at the lower boundary. Runs on finer grids were carried out for many parameter choices to check convergence. Whilst the grid spacing changes significantly in absolute terms, the variation between adjacent grid points is always less than 2% so that the grid is close to uniform.

Finally, the initial conditions generated by the above process are used as the input for a long run simulation with no additional sources which is run until residual velocities become negligible. This final configuration, which contains velocities of no more than 0.1% of the local sound and Alfvén speeds at all locations, is then used as the equilibirum for all simulations.

4.3. Alfvén wave driver

Alfvénic disturbances are launched by the addition of a random driver to the right hand side of Eq. (7), taking the following form:

$$F(z,t) = A_1\, A_2(t)\, {\rm e}^{-[(z-z_0)/L]^2}. \tag{29}$$

There are four parameters associated with this driver; A_1 governs the initial amplitude of the Alfvénic disturbances, z_0 is the input height of the driver in the atmosphere, A_2 is a time-varying random number between −1 and 1 and L controls the spatial extent over which the driver acts. Figure 3 shows a typical angular velocity profile generated by this driver. The velocity at the base of the photosphere is typically 0.5−2 km s^{-1}, in keeping with with observed photospheric motions.

4.4. Numerical technique

Equations (6)–(10) are solved using the Versatile Advection Code (VAC) developed by Tóth (1996). Of the numerous numerical schemes implemented by this code, we have chosen to use the two flux corrected transport (FCT) schemes. In essence, FCT schemes proceed by adding a weighted combination of a low- and a high-order numerical solution at each time step. The weighting attempts to retain as much of the accuracy of the high order scheme as possible whilst avoiding the trailing ripples such schemes tend to produce behind steep gradients. They are very effective in coping with sharp gradients and are thus excellent for non-linear modeling in general and shock capturing in particular. The interested reader is directed to Book (1981) for further details.

5. Results

In Paper I, we showed that a continuous sinusoidal driver results in continuous interaction between the driven upwardly propagating wave train and the downward propagating reflected wave train. Once the first reflected wave reaches the wave source, a partially standing wave pattern will be formed. This will not be a true standing wave since the amplitude of the reflected waves are reduced compared to the driven waves and also the point of reflection, the transition region, is not stationary. To study the implications of this, we consider an extremely simplified analysis; a superposition of two waves with equal frequency propagating in opposite directions in an homogeneous atmosphere:

$$B_x = B_1 \cos(\omega t - kx) + B_2 \cos(\omega t + kx). \tag{30}$$

It is trivial to show that in this case the Lorentz force is given by

$$\frac{\partial B_x^2}{\partial x} = kB_1^2 \sin\left(2\left(\omega t - kx\right)\right) - kB_2^2 \sin\left(2\left(\omega t + kx\right)\right) + 2kB_1B_2 \sin(2kx). \tag{31}$$

The first two terms produce no net force over one wave period. The last term produces a periodic force with spatial wavelength of half the Alfvén wavelength. In the chromosphere, the plasma beta is of the order of 0.01 and magnetic forces dominate. The force crudely described above would be expected to drive plasma toward the nodes and away from the troughs of the standing wave pattern until it is countered by the plasma pressure gradient. This effect was directly observed in Paper I.

It was assumed that a random source of Alfvénic disturbances would significantly reduce this effect. In fact, this assumption is not necessarily correct. To see why, we can extend the simple analysis above to the case of random Alfvénic disturbances as follows. Firstly, we transform coordinates to

$$\phi_1 = x - v_A t,\ \phi_2 = x + v_A t. \tag{32}$$

Functions of ϕ_1 and ϕ_2 then describe upward and downward propagating disturbances, respectively. We begin by writing a general disturbance as a superposition of an upward and downward propagating disturbance,

$$B_x = f_1(\phi_1) + f_2(\phi_2). \tag{33}$$

Next, we Fourier analyse over ϕ_1 or ϕ_2 as appropriate:

$$B_x = \int_{-\infty}^{\infty} F_1(k_1) \mathrm{e}^{-2i\pi k_1 \phi_1} \mathrm{d}k_1 + \int_{-\infty}^{\infty} F_2(k_2) \mathrm{e}^{-2i\pi k_2 \phi_2} \mathrm{d}k_2. \tag{34}$$

From here on, the region of integration is always $-\infty$ to $+\infty$ unless otherwise specified. The Lorentz force is obtained by squaring and differentiating with respect to x:

$$\begin{aligned} F &= \iint g(k_1, \overline{k}_1) F_1(k_1) F_1(\overline{k}_1) \mathrm{e}^{g(k_1,\overline{k}_1)\phi_1} \mathrm{d}k_1 \mathrm{d}\overline{k}_1 \\ &+ \iint g(k_2, \overline{k}_2) F_2(k_2) F_2(\overline{k}_2) \mathrm{e}^{g(k_2,\overline{k}_2)\phi_2} \mathrm{d}k_2 \mathrm{d}\overline{k}_2 \\ &+ 2 \iint g(k_1, k_2) F_1(k_1) F_2(k_2) \mathrm{e}^{-2i\pi(k_1\phi_1 + k_2\phi_2)} \mathrm{d}k_2 \mathrm{d}\overline{k}_2, \end{aligned} \tag{35}$$

where $g(a, b) = -2i\pi(a + b)$. The first two integrals express the Lorentz force contribution due purely to the upward and downward propagating components respectively whilst the last integral represents the force produced by the interaction of the two components. The time averaged (over time τ) Lorentz force for the first two components is:

$$\begin{aligned} I_1 &= \frac{1}{v_A \tau} \iint F_1(k_1) F_1\left(\overline{k}_1\right) \mathrm{e}^{g\left(k_1,\overline{k}_1\right)x_0} \left(1 - \mathrm{e}^{-g\left(k_1,\overline{k}_1\right)v_A\tau}\right) \mathrm{d}k_1 \mathrm{d}\overline{k}_1 \\ &+ \frac{1}{v_A \tau} \iint F_2(k_2) F_2\left(\overline{k}_2\right) \mathrm{e}^{g\left(k_2,\overline{k}_2\right)x_0} \left(\mathrm{e}^{g\left(k_2,\overline{k}_2\right)v_A\tau} - 1\right) \mathrm{d}k_2 \mathrm{d}\overline{k}_2. \end{aligned} \tag{36}$$

All contributions within the integrals are oscillatory in time and clearly $\lim_{\tau\to\infty} I_1 = 0$. However, integrating the third component yields:

$$\begin{aligned} I_2 &= \frac{1}{v_A \tau} \iint \frac{F_1(k_1) F_2(k_2)(k_1 + k_2)}{k_1 - k_2} \\ &\times \mathrm{e}^{g(k_1,k_2)x_0} \left(\mathrm{e}^{g(k_1,-k_2)v_A\tau} - 1\right) \mathrm{d}k_1 \mathrm{d}k_2. \end{aligned} \tag{37}$$

For small $k_1 - k_2$,

$$\frac{1}{(k_1 - k_2)v_A\tau} \left(\mathrm{e}^{g(k_1,-k_2)v_A\tau} - 1\right) \approx -2i\pi. \tag{38}$$

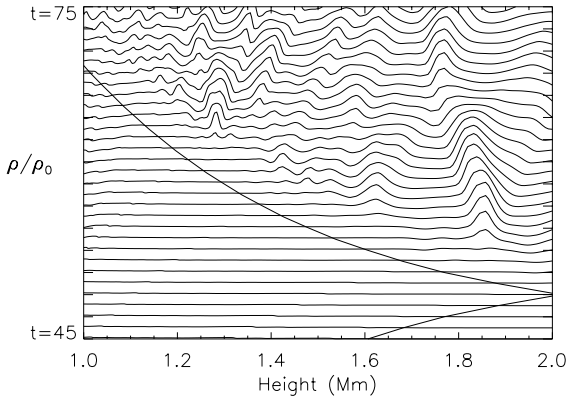

Fig. 4. Development of density profile caused by interaction of upward propagating driven waves with downward propagating waves reflected at the transition region. The figures shows a stack of plots of the ratio of the density to initial density between $t = 45$ s and $t = 75$ s. The dark line shows the position of the front of the upward propagating disturbance and the estimated position of the downward propagating disturbance formed by reflection at the transition region at 2.2 Mm. Each plot is separated by 0.5 on the vertical axis both in density ratio and time.

Thus the interaction of upward and downward propagating disturbances (expressed by I_2) results in regions of approximately time independent Lorentz force which are not present for disturbances propagating in one direction only (expressed by I_1).

As with a simple standing wave, this can lead to density perturbations, the precise location and magnitude of which will depend on the form of the disturbances (equivalently the form of F_1 and F_2).

Figure 4 shows the evolution of the density profile for a typical simulation. The curved line shows the position of the front of the wave train before and after reflection at the base of the transition region, which is located just above the spatial domain shown at 2200 km. The position of the reflected train is estimated under the assumption that it propagates at the same speed as the upward propagating train. That the density is unaffected by the initial passage of the upward propagating disturbances means this is probably a reasonable assumption, but in any case it is only shown for convenience. After approximately 47 s, the leading edge of the Alfvénic disturbance reaches the transition region. Roughly 75% of the disturbance amplitude is reflected (the rest being transmitted) and propagates downward, interacting with the driven disturbances still propagating upward. In accordance with the above analysis, the Lorentz force then deforms the initially smooth density profile into regions of locally high and low density within about 5 s of the reflected disturbance passing.

Sharp gradients also appear in the sound speed profile which facilitate the steepening of vertical velocity perturbations into slow shocks. These shocks impact sporadically on the transition region, which is moving following the initial impact of the Alfvénic disturbances, repeatedly propelling it upwards. The "spicule" dynamics are driven by the same mechanism as in Paper I, the key difference being that the random driver gives rise to an irregular density perturbation whereas the simple

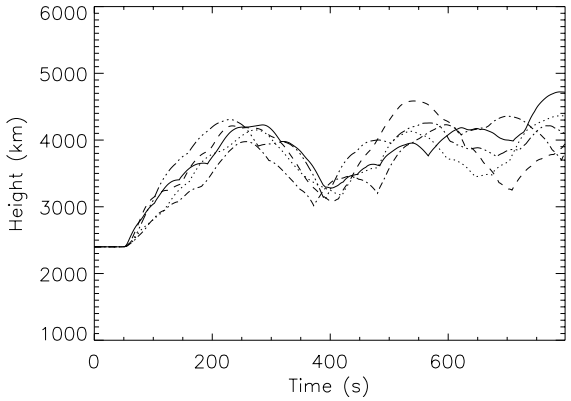

Fig. 5. Transition region position against time for various runs with a random driver with both heating and damping included. Parameters were identical for all simulations.

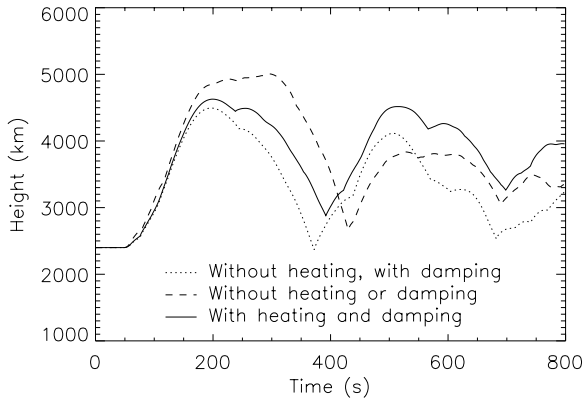

Fig. 6. Transition region position against time for a random driver with and without heating and damping.

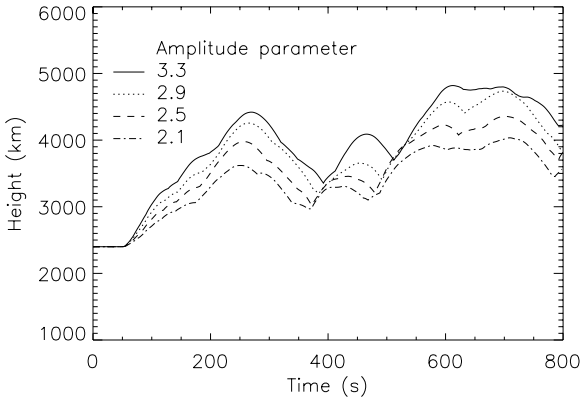

Fig. 7. Transition region position against time for varying amplitude. All other parameters are identical.

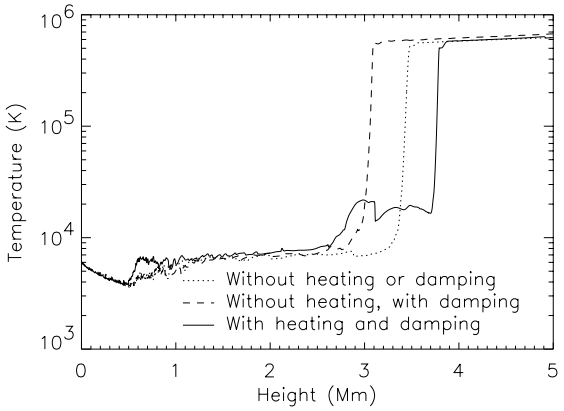

Fig. 8. Final temperature profiles with and without heating for the simulations in Fig. 6.

sinusoidal driver caused peaks and troughs in the density with a regular spatial separation of half the local Alfvén wavelength at the frequency of the driver. Figure 5 shows the transition region position against time for some typical examples generated by our numerical scheme. The successive slow shock impacts can be seen as bumps in the profiles.

Figure 6 shows the effect of including heating and damping. The strength of the initial rise is governed primarily by the amplitude of the disturbance when it impacts the transition region. Consequently, this rise is reduced when damping is switched on. Heating increases support for the structure provided by the thermal pressure gradient, leading to greater heights by the end of the simulation. Figure 8 shows the final temperature profiles in each case. The partially ionised state of the chromosphere allows the ionisation energy to act as a source and sink for energy input. As a result, the expansion of the structure is roughly isothermal when heating from ion-neutral damping is not included. When the heating is included, an extended region of the upper chromosphere is heated up to temperatures of 10 000–20 000 K. Because the heating mechanism relies on the presence of both ions and neutrals, it becomes negligible above temperatures of 10 000 K where the hydrogen is completely ionised. Any further heating at these temperatures occurs solely due to shock heating; for example a shock front is clearly evident just above 3 Mm in Fig. 8.

Figure 7 shows the effect of increasing the amplitude of the Alfvénic disturbances. Unsurprisingly, the trend is for increasing heights with increasing amplitude due to the increased strength of both the initial impact and increased shock strength.

Figure 9 compares the dynamics of the random and periodic driver cases. The slow shock impacts in the periodic case are regularly spaced. With the random driver, the plasma is able to fall under gravity between the rarer significant impacts. Heights of the structures formed are slightly lower for equivalent wave energy input, as measured by the average value of v_θ^2 just before the initial disturbance reaches the transition region.

Figure 10 compares the typical temperature profiles formed by the end of the simulation for both periodic and random drivers. Heating is as significant with a random disturbance as with a periodic disturbance. In both cases, there is a large region below the transition region which has been heated to above 10 000 K. At these temperature, Hydrogen becomes completely ionised. Consequently, the ion slip drops to negligible levels and no further heating by ion-neutral damping can occur. The "lumpiness" in the profiles is caused by the passage of slow shocks and is evident in both cases.

6. Conclusion

Many proposals for the generation of solar spicules have been put forward. Haerendel (1992), suggested that already formed

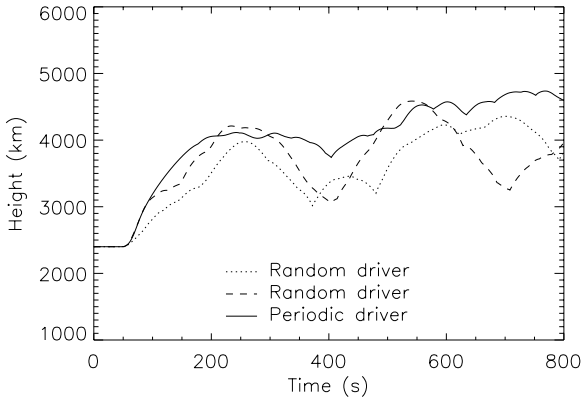

Fig. 9. Transition region position against time comparing the random driver with a periodic driver.

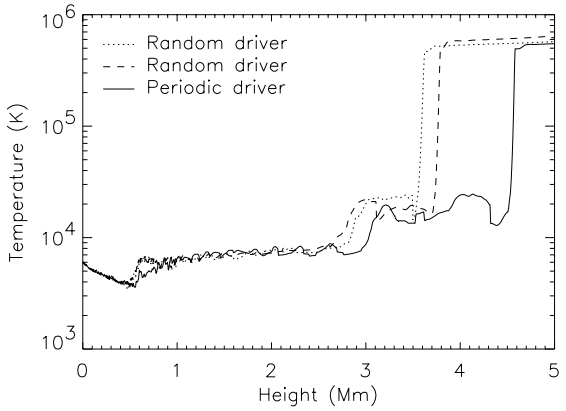

Fig. 10. Final temperature profiles for both random and periodic driver simulations.

spicules can be supported against gravity by momentum transfer of Alfvén waves into the vertical direction via ion-neutral damping. Further theoretical calculations under the WKB approximation on plane polarised linear waves (De Pontieu & Haerendel 1998) strengthened this as a possibility. De Pontieu (1999) subsequently tested this hypothesis numerically, again under the WKB assumption, and found that spicule-like structures could not only be supported by this mechanism as theorised, but also generated. The obvious extension was to remove the WKB assumption, which is invalid in the transition region at the frequencies concerned. This was carried out in Paper I.

It was found that interaction between the driven upward propagating wave train and downward propagating wave train reflected by the transition region resulted in stratification of the atmosphere into high and low density regions. Slow shocks are generated which subsequently impact on the transition region, periodically pushing it upward. Under these conditions, which were substantially different from those under which the theoretical model is derived, there was little evidence of the proposed momentum transfer mechanism in the spicule dynamics. It was thought that the density deformation was a consequence of the monochromatic nature of the driver and that a random driver would much reduce the effect. Results of simulations with such a driver are presented in this paper. The deformation of the chromosphere still occurs, although with a far less regular structure, and the dynamics are still driven by slow shocks formed about these local peaks and troughs in density. However, the extent of the deformations and strength of the shocks is lower. That this deformation still occurs to such an extent is worth noting. It seems to be a natural and unavoidable consequence of Alfvénic disturbances propagating in the solar atmosphere.

Significant heating and damping still occurs. This further strengthens the suggestion made in Paper I that careful consideration should be made before deciding to neglect this effect as most previous numerical models have done although a treatment of radiative losses must be included before this conclusion can be firmly drawn. The similarity of final heights in the case when damping is included or excluded without heating raises the possibility that there is some net upward component of the Lorentz force contributed by the inclusion of ion-neutral damping, although it appears this is still a relatively minor effect.

As in Paper I, the structures formed show similarities with spicules in terms of densities and temperatures. Whilst the lower end of the observable height range can be recreated, it is very unlikely that the tall spicules observed above the solar limb can be generated by this mechanism, especially since including radiative losses is likely to damp the slow shocks and reduce heights further. However, low-lying spicules which are believed to make up the continuum are easily generated. These low heights are the common failing of most numerical models (when more realistic physics is included). On the other hand, these models can all generate low-lying spicules without resorting to unrealistic input parameters. In attempting to match the heights of the spicules observed on the solar limb, observations which automatically pre-select the tallest and most vertical spicules, modellers may have overlooked the possibility they have found explanations for the smaller and more abundant spicules that make up the continuum.

Finally, the environment within flux tubes is not well known. Preliminary simulations suggest the results are quite sensitive to the equilibrium conditions. The final paper in this series will address this issue as well as including simple treatments of radiation and thermal conduction, important as the ionslip term is particularly sensitive to changes in temperature at chromospheric temperatures.

Acknowledgements. This work was supported by Particle Physics and Astronomy Research Council (PPARC) grant PPa/S/S/2000/02983. R.E. acknowledges M. Kéray for patient encouragement and the financial support obtained from the NSF, Hungary (OTKA, Ref. No. TO43741) and The Royal Society (Ref. No. 15599).

References

Allen, C. W. 1963, Astrophysical Quantities (Athlone Press)
Beckers, J. M. 1972, ARA&A, 10, 73
Book, D. L. 1981, Finite-Difference Techniques for Vectorized Fluid Dynamics Calculations (Springer-Verlag), 29
Brown, J. C. 1973, Sol. Phys., 29, 421
Budnik, F. 1998, A&A, 334, L77
Cheng, Q.-Q. 1992a, A&A, 266, 537
Cheng, Q.-Q. 1992b, A&A, 266, 549

Cheng, Q.-Q. 1992c, A&A, 262, 581
Cowling, T. G. 1976, Magnetohydrodynamics (Hilger)
De Pontieu, B. 1996, Ph.D. Thesis, University of Ghent, Belgium
De Pontieu, B. 1999, A&A, 347, 696
De Pontieu, B., & Haerendel, G. 1998, A&A, 338, 729
De Pontieu, B., Erdélyi, R., & de Wijn, A. G. 2003, ApJ, 595, L63
De Pontieu, B., Erdélyi, R., & James, S. P. 2004, Nature, 430, 536
Haerendel, G. 1992, Nature, 360, 241
Hasan, S. S., & Keil, S. L. 1984, ApJ, 283, 75
Hollweg, J. 1982, ApJ, 257, 345
Hollweg, J. V., Jackson, S., & Galloway, D. 1982, Sol. Phys., 75, 35
Kudoh, T., & Shibata, K. 1999, ApJ, 514, 493
James, S. P., & Erdélyi, R. 2002, A&A, 393, L11
James, S. P., Erdélyi, R., & De Pontieu, B. 2003, A&A, 406, 715
Lynch, D. K., Beckers, J. M., & Dunn, R. B. 1973, Sol. Phys., 30, 63
Matsuno, K., & Hirayama, T. 1988, Sol. Phys., 117, 21
Mitchner, M., & Kruger Jr, H. 1973, Partially Ionised Gases (Wiley-Interscience)
Nishikawa, T. 1988, Publ. Astron. Soc. Japan, 40, 13
Osterbrock, D. E. 1961, ApJ, 143, 904
Pasachoff, J. J., Noyes, R. W., & Beckers, J. M. 1968, Sol. Phys., 5, 131
Pishkalo, M. I. 1994, Astron. Nachr., 5, 391
Ruždjak, V. 1977, Bull. Astron. Inst. Czech., 28, 198
Sterling, A. C. 2000, Sol. Phys., 196, 79
Sterling, A. C., & Hollweg, J. V. 1988, ApJ, 327, 950
Sterling, A. C., & Mariska, J. T. 1990, ApJ, 349, 647
Suematsu, Y., Shibata, K., Nishikawa, T., & Kitai, R. 1982, Sol. Phys., 75, 99
Tóth, G. 1996, Astrophys. Lett. Commun., 34, 245
Vernazza, J. E., Avrett, E. H., & Loeser, R. 1981, ApJ, 45, 635